

# Silicon Quantum Dots: Photoluminescence Controlling and Solar Cell Application

Wen Zhong Shen\*

Laboratory of Condensed Matter Spectroscopy and Opto-Electronic Physics, and Key Laboratory of Artificial Structures and Quantum Control (Ministry of Education), Department of Physics, and Institute of Solar Energy, Shanghai Jiao Tong University, 800 Dong Chuan Road, Shanghai, People's Republic of China 200240

## ABSTRACT

In this invited paper, we report the effect of different annealing environments on the changeable radiative recombination characteristics of Si quantum dots (QDs), which not only provides ways to identify the photoluminescence mechanism, but also realizes the possibility to control the origin of the luminescence. We also focus on the application of Si QDs in the third-generation solar cells, with the emphasis on growth of well-ordered Si QDs, on photoresponse control of Si QDs, and on approaches to reduce the lattice thermalization loss in Si QDs solar cells.

**Keywords:** Si quantum dots, photoluminescence controlling, solar cell application, PECVD

## 1. INTRODUCTION

It is well known that poor optical properties in bulk silicon (Si) have prevented it from application in devices such as light-emitting diodes and lasers. The observation of efficient light emission at visible wavelengths in porous Si nanostructures (through simple electrochemical etching of crystalline Si in hydrofluoric acid in 1990 [1]) has created huge interest among scientists and engineers. Thousands of papers on light emission from nanoscale Si structures have been published since then, but the origins of this photoluminescence (PL) have been the subject of intense debate for almost two decades. Recently, Godefroo *et al.*, [2] have demonstrated that the PL from Si quantum dots (QDs) annealed in active hydrogen ambient originates mainly from quantum confinement effect (QCE) due to the drastically decreased defects density, and the light emission mechanism converts to radiative defect states by using ultraviolet illumination to drive out the hydrogen (i.e., reintroduce the defects).

On the other hand, current third-generation approaches to photovoltaics (PVs) aim to decrease costs to well below the \$1.0/W level of thin-film-based second-generation PVs to \$0.5/W, potentially to \$0.2/W or better, by significantly increasing efficiencies but maintaining the economic and environmental cost advantages of thin-film deposition techniques. For amorphous Si thin-film solar cells, the best performance in laboratory is efficiencies of 14.6% initial and 13.0% stable under AM 1.5 over a 0.25cm<sup>2</sup> active area cell, but the large scale manufacturing efficiencies ~8.0-9.6% [3]. Light-induced degradation caused by the Staebler-Wronski effect is the main challenge in amorphous Si thin-film solar cells. Si nanotechnology is the best choice to improve the metastabilities and to increase the quantum efficiency.

Here, we will address the origin of visible luminescence in hydrogenated amorphous Si nitride, controlling the red luminescence from Si QDs, and application of Si QDs in the third-generation solar cells.

## 2. ORIGIN OF VISIBLE LUMINESCENCE IN AMORPHOUS SILICON NITRIDE

In this section, the Si nanostructure we are interested in is hydrogenated amorphous Si nitride ( $\alpha$ -SiN<sub>x</sub>:H) films embedded with Si QDs, which represent good candidates for Si-based light-emitting devices due to the relatively low barrier (~2.0eV) for carriers [4]. The samples were deposited by using a low frequency (440kHz) plasma enhanced chemical vapor deposition (PECVD) system on ~0.5mm thick p-type crystalline Si substrates (thickness of ~350-

\* E-mail: wzshen@sjtu.edu.cn, phone & fax: 86-21-5474755

380nm). Precursor gases were  $\text{NH}_3$  and  $\text{SiH}_4$  with a constant  $\text{NH}_3/\text{SiH}_4$  flux ratio of 1700/455. We label samples Sx ( $x=1, 2, 3, 4$ ) for deposition temperature  $T_d$  at 200, 300, 400, and 500°C, respectively.

Figure 1(a) presents the room-temperature PL spectrum of a typical sample S2, which was obtained on a Jobin Yvon LabRAM HR 800 UV micro-Raman spectrometer using 325nm line of He-Cd laser. We have decomposed the PL spectrum into three Gaussian peaks, and these PL bands are found to exhibit different characteristics under different  $T_d$ . In the near-infrared to red light range, the Gaussian peak in S1 is almost negligible, while those of S2-S4 exhibit an obvious redshift from 1.91 in S2 to 1.74eV in S4. The green PL peak shifts continuously toward the low energy side from 2.40 to 2.05eV in S1-S4. In contrast, the blue PL peak energy keeps almost unchanged ( $3.00\pm 0.05\text{eV}$ ).

Figure 1(b) shows the Raman spectrum of the sample S2, which was recorded under back scattering configuration in the same system as for the PL spectra. It is clear that the narrow transverse optical (TO) band at about  $520\text{cm}^{-1}$  comes from the crystalline Si substrate, while the longitudinal optical (LO) band centers around  $385\text{cm}^{-1}$ . Another  $\text{TO}_1$  band is at  $\sim 492\text{cm}^{-1}$ , where the typical Raman spectrum of amorphous Si QDs lies. With the increase of  $T_d$ , the  $\text{TO}_1$  peak shifts from 492 to  $498\text{cm}^{-1}$ , suggesting the increase of the Si QDs size ( $\sim 1.7\text{nm}$ ).

Figure 1(c) illustrates the cross-sectional high resolution transmission electron microscopy (HRTEM, JEOL JEM-2100F) image of sample S2. We note that the Si QDs with higher density than the Si nitride matrix appear as dark spots. The average dot size is found to be  $\sim 3.1\text{nm}$  for sample S2, which is in good agreement with the size of  $\sim 3.0\text{nm}$  for the red emission according to the QCE model [4]. As we know, Si-H bonds can be broken to provide the Si nucleus for the formation of the Si QDs. Under higher  $T_d$ , the Si-H bonds are easier to be broken, leading to a higher Si concentration in the film. The formed Si QDs will congregate and grow up with. On the other hand, hydrogen-related bonds decrease due to more  $\text{NH}_3$  effusing, and could not passivate well the nonradiative defects existing at the interface between Si QDs and SiN matrix, leading to the observed decrease of PL intensity from samples S1 to S4.

We have further carried out the ultraviolet reflection measurements [Fig. 1(d) for sample S2] in the range of 3.1-4.7eV using a Jobin Yvon 460 monochromator for the origin of the green PL. With the help of the Tauc-Lorentz-Urbach model [5] (solid curve), the yielded optical band gap ( $E_g$ ) and Urbach tail ( $E_U$ ) have been found to decrease with increasing  $T_d$  due to the decrease of N/Si ratio, therefore, leading to the significant redshift of the green PL peak.  $E_U$  decreases monotonically with the enhancement of  $T_d$ , suggesting that narrower bandtail and more ordered silicon nitride network can be achieved at higher  $T_d$ . On the basis of the redshift of peak position, narrowing of bandwidth and temperature quenching of luminescence, we attribute the green emission to the bandtail recombination of carriers.

As for the blue band, we can assign it to the electronic transitions of  $\equiv\text{Si}^0 \rightarrow \equiv\text{Si}-\text{Si}\equiv$ . We make the assignment based on (1) tight-binding method for gap states in SiN. The states of  $\equiv\text{Si}^0$  and  $\equiv\text{Si}-\text{Si}\equiv$  lie about 3.1 and 0.1eV above the valence band, respectively, the radiative recombination between the two states can generate the PL peak at  $\sim 3.0\text{eV}$ , and (2) dependence of the defect-related PL intensity on  $T_d$ . With the increase of  $T_d$ , the  $\equiv\text{Si}^0$  dangling bonds and  $\equiv\text{Si}-\text{Si}\equiv$  units would decrease due to the increase of the Si-N bonds induced by the severe nitridation process. Higher  $T_d$  will also hinder the diffusion of hydrogen, which decreases significantly the randomness of the SiN network, resulting in fewer silicon defects. The blue PL intensity is found to decrease significantly with increasing  $T_d$ , as expected.

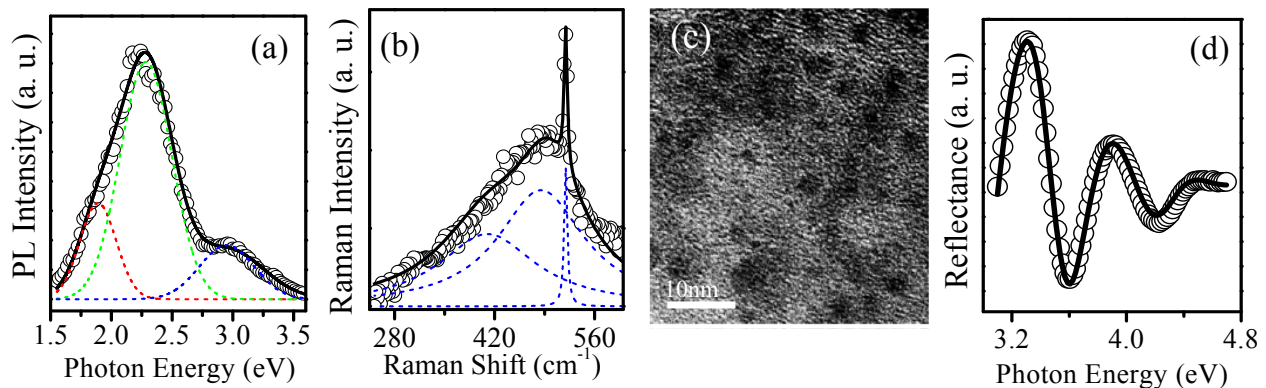


Figure 1. Structural and room-temperature optical properties of  $\alpha\text{-SiN}_x\text{:H}$  sample S2 embedded with Si QDs. (a) PL spectrum, (b) Raman spectrum, (c) cross-sectional HRTEM image, and (d) ultraviolet reflection spectrum.

### 3. CONTROLLING THE RED LUMINESCENCE FROM SILICON QUANTUM DOTS

The structure and surface chemistry of the Si QDs determine the nature of the luminescence. We show in this section the controlling of the red luminescence through a simple and effective annealing treatment technique to modify the Si QDs size, density, and chemical configurations. Fig. 2(a) shows the room-temperature red luminescence from sample S3 under different annealing temperature  $T_A$  of 30min in Argon ambient. An obvious redshift from 1.82eV in the as-deposited sample to 1.76eV in the one with  $T_A=800^\circ\text{C}$ , accompanied with a strong enhancement of the luminescence intensity by a factor of 15. The PL peak exhibits a continuous redshift from 1.76 to 1.70eV with the further increase of  $T_A$  to  $1100^\circ\text{C}$ , however, the luminescence intensity decreases drastically. With the decrease of measured temperature, a significant redshift of the luminescence peak occurs annealed below or at  $800^\circ\text{C}$ , while the PL peak remains almost unchanged under higher  $T_A$ . The other samples exhibit the similar annealing temperature behavior.

The HRTEM observes the evolution of the Si QDs size and density with  $T_A$ . The average dot size increases from  $\sim 3.6\text{nm}$  in the as-deposited sample to  $\sim 4.9\text{nm}$  in the annealed one at  $800^\circ\text{C}$ , while the observed enhancement of the Si QDs density from  $7.6 \times 10^{12}$  to  $1.1 \times 10^{13}\text{cm}^{-2}$  explains the increase of the PL intensity annealed below/at  $800^\circ\text{C}$ . With the further increase of  $T_A$  to  $1100^\circ\text{C}$ , the average dot size increases drastically to  $\sim 9.8\text{nm}$  with the density of  $2.5 \times 10^{12}\text{cm}^{-2}$ . With increasing  $T_A$ , the Raman peak shifts toward the higher energy and the linewidth becomes narrower, both of which indicate the increase of Si QDs size. Therefore, annealing treatments contribute to create new Si QDs and increase the size of already existing Si QDs. However, when  $T_A$  increases over  $800^\circ\text{C}$ , the coalescence, overgrowth, and expansion of Si QDs will significantly reduce the dot density, but still increase the dot size. As a result, at  $T_A \leq 800^\circ\text{C}$ , the red luminescence peak position agrees well with the QCE model. Large Si QDs under  $T_A > 800^\circ\text{C}$  result in high interface state density. Considering the temperature-independence of the luminescence peak and the complete effusion of hydrogen, we can assign the red PL to the electrons trapped at localized states there.

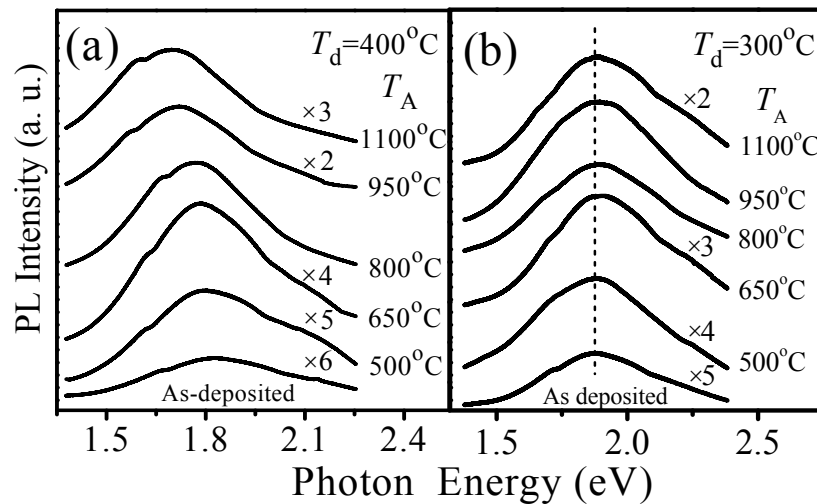


Figure 2. Room-temperature red luminescence of  $\alpha\text{-SiN}_x\text{:H}$  embedded with Si QDs under different annealing temperature  $T_A$  of 30min. (a) Sample S3 in Argon ambient, (b) sample S2 in oxygen ambient.

As we know, in the hydrogen environment, annealing treatment can reduce drastically the radiative defects density (passivation), which would make QCE dominant in the PL [2]. Compared with argon and hydrogen, oxygen is more active and can react easily with both Si and nitrogen, resulting in more complicated SiN network. The changeable radiative recombination characteristics of Si QDs in different annealing environments are very useful to control the nature of the red luminescence. Fig. 2(b) presents the room-temperature red luminescence from sample S2 under different annealing temperature  $T_A$  of 30min in oxygen ambient. With the increase of  $T_A$ , the emission peak centered at 1.9eV keeps unchanged. However, in the Raman spectra, we can still observe the blueshift of the  $\text{TO}_1$  peak the narrowing of the full width at half maximum (FWHM), indicating the increase of Si QDs size. Furthermore, both the PL peak energy and FWHM are almost independent of temperature throughout the measured range. These observations indicate that the mechanism of light emission in the oxidized samples is not determined by the size dependent QCE.

In time-resolved PL measurements, we have observed a double exponential function: the faster decay component increases from 0.80 to 0.93ns, and the longer decay one from 1.73 to 4.70ns with the increase of  $T_A$ . First principles calculations have revealed that the nanosecond decay time can be attributed to the localized states excitons transition at the surface of the Si QDs, where the faster and longer decay components correlate to the nonradiative excitons trapping time on the localized states and the recombination (both radiative and nonradiative) of the trapped excitons, respectively [6]. Therefore, the red luminescence of the oxidized samples originates from the localized excitons radiative recombination via the surface states of the Si QDs related to the Si-N or Si-O-Si bonds. Our above results clearly demonstrate that annealing treatment in different environments (Argon, hydrogen, and oxygen) is a simple and effective technique to control the origin of the PL in Si QDs from QCE to localized interface/surface states and vice versa via the radiative defects density.

#### 4. APPLICATION OF SILICON QUANTUM DOTS IN THIRD-GENERATION SOLAR CELLS

For the application of the third-generation solar cells, we discuss the hydrogenated nanocrystalline Si (nc-Si:H) thin film, which is a mixed material comprised of an amorphous Si phase and crystalline Si grains with a wide range of crystalline volume fraction. We have also employed the PECVD technique to grow nc-Si:H thin films at a temperature of 250°C and radio frequency of 13.56MHz. During the growth, the hydrogen has been found to play an important role. The role of H from atomic-scale mechanism is that the insertion of H atoms into strained Si-Si bonds, forming intermediate bond-centred Si-H-Si configurations. The strained Si-Si bonds are either break or relax, undergo local structural rearrangements that result in bond lengths and angles closer to those of c-Si, i.e., hydrogen leads to disorder-to-order transitions [7]. By proper controlling the interaction between hydrogen and Si atoms in the growth, we have realized the well-ordered nc-Si:H thin films with efficient room-temperature luminescence, high electron mobility ( $>100\text{cm}^2/\text{Vs}$ ), and novel quantum transport phenomena [8-10]. The nc-Si:H thin films are composed of ~50% small nanocrystalline Si (mean grain size of 3-6nm) and 50% a-Si tissues in the thin interface regions (thickness about 2-3 atomic spacing) among the grains.

Figure 3(a) presents the room-temperature photocurrent spectrum of a typical nc-Si:H thin film (thickness of ~1.0 $\mu\text{m}$ ) doped with phosphine ( $\text{PH}_3/\text{SiH}_4$ ) of ~0.8% on the glass substrate. Compared with the bulk Si, strong optical absorption and high photocurrent are found in nc-Si:H thin films and attributed to the enhancement of the optical absorption cross section and good carrier conductivity in the nanometer grains. High photocurrent response may facilitate the fabrication of nc-Si:H thin film solar cells. Furthermore, both the thin film uniformity and structural properties, i.e., the distribution of grain sizes and crystalline volume fraction, with different doping concentrations are revealed and physically interpreted on the basis of growth mechanism. We have observed broader photocurrent response in Si quantum dots with larger size dispersion due to the improvement of light harvest. As a result of tunneling loss in the expanded energy distribution, there is a tradeoff between the absorption enhancement and reduced transport for the photocurrent intensity. Therefore, we can tune the photoresponse through size distribution control of Si QDs.

The tandem scheme for thin film solar cells uses a stack of cascaded multiple p-n junctions with band gaps better matched to the solar spectrum from about 0.5 to 3.5eV. The bandgap engineering (1.2-2.4eV) of the nc-Si:H thin films can be easily realized by the QD size and the doping concentration. Higher-energy photons are absorbed in the higher-band-gap nc-Si:H and lower-energy photons in the lower-band-gap nc-Si:H, reducing the overall heat loss due to carrier relaxation via phonon emission. In addition to the tandem scheme for the Si QDs solar cells, there are two kinds of novel nc-Si:H thin film solar cells for hot carrier scheme utilizing the hot carriers before they relax to the band edge via phonon emission. The first approach is the hot carrier transport through minibands. Fig. 3(b) shows the successful explanation (solid curves) of the photocurrent by the classical theory due to the phonon-assisted transition, indicating that the energy band of the continuous states is also formed in the nc-Si:H thin film like that in c-Si. The photocurrent structure from the transitions of the Si-like continuous energy band is very narrow in terms of the energy width (linewidth 300meV), but is quite larger than the phonon energy of nc-Si:H thin film, which means a miniband. In the nc-Si:H, the high density of nanometer grains embedded in the very thin a-Si:H boundaries that results in a superposition of a miniband with a Si-like band gap in the tail band of a-Si:H. The observed minibands in nc-Si:H thin films could be expected to slow the carrier cooling and permit the transport and collection of hot carriers at the respective p and n contacts to produce a higher photopotential.

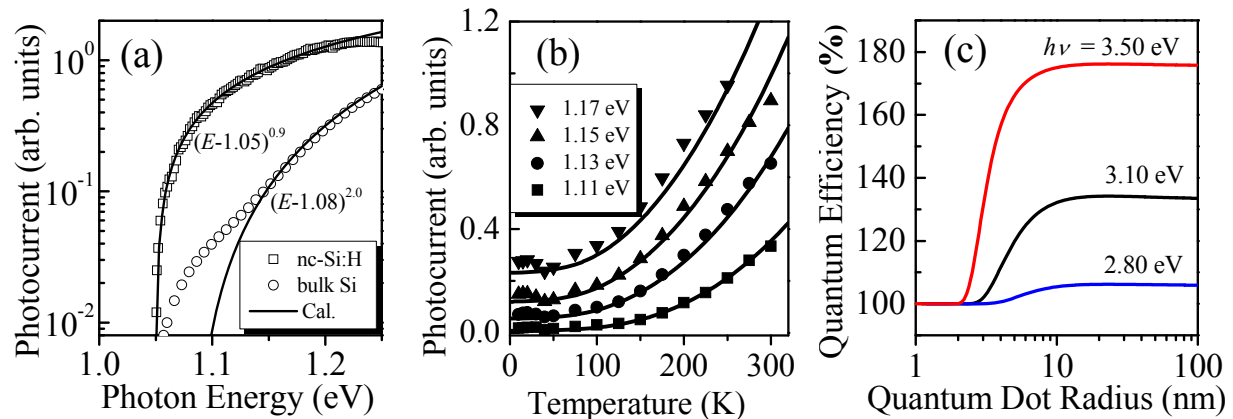


Figure 3. (a) Room-temperature photocurrent spectrum of a typical nc-Si:H thin film on glass substrate, together with that of bulk Si for comparison. (b) Temperature dependent photocurrent for nc-Si:H thin film on Si substrate. (c) Calculated quantum efficiency of Si QDs as a function of dot radius  $R$  at the energy relaxation time  $t_s=50$ fs under different pump photon energies  $h\nu$ .

The second possibility is the new concept multiple exciton generation (MEG) solar cells. In conventional solar cells, absorption of a single photon produces a single exciton, the photon excess energy is dissipated as heat via phonon emission. However, it has been found that the number of excitons produced by a single photon is only limited by energy conservation, photons with energies  $E_g$ ,  $2E_g$ , and  $3E_g$  produce one, two, and three excitons, respectively [11]. The corresponding quantum efficiency (QE) is described by a staircaselike spectral dependence, in which QE increases by 100% when the photon energy is increased by  $E_g$ . Highly efficient MEG effect (the quantum yield of excitons produced per absorbed photon reaches 2.6 at  $3.4E_g$ ) in colloidal Si nanocrystals has been reported at lower photon energies in the visible region [12], which opens the possibility to expand to nc-Si:H films for MEG cells with increasing power conversion efficiency. Fig. 3(c) illustrates the calculated quantum efficiency of Si QDs, based on the Fermi statistical theory and the impact ionization mechanism, as a function of dot radius  $R$  at the energy relaxation time  $t_s=50$ fs under different pump photon energies  $h\nu$ . The result shows that it is feasible to improve the efficiency of nc-Si:H solar cells by using the MEG effect.

### ACKNOWLEDGMENTS

This work was supported partially by Natural Science Foundation of China under contract of 10734020 and 11074169, and National Major Basic Research Projects of 2010CB933702.

### REFERENCES

- [1]. Canham, L. T., "Silicon quantum wire array fabrication by electrochemical and chemical dissolution of wafers," *Appl. Phys. Lett.* 57(10), 1046-1048 (1990).
- [2]. Godefroy, S., Hayne, M., Jivanescu, M., Stesmans, A., Zacharias, M., Lebedev, O. I., Tendeloo, G. V. and Moshchalkov, V. V., "Classification and control of the origin of photoluminescence from Si nanocrystals," *Nature Nanotech.* 3, 174-178 (2008).
- [3]. Yang, J., Yan, B. J. and Guha, S., "Amorphous and nanocrystalline silicon-based multi-junction solar cells," *Thin Solid Films* 487(1-2), 162-169 (2005).
- [4]. Park, N. -M., Choi, C. -J., Seong, T. -Y. and Park, S. -J., "Quantum confinement in amorphous silicon quantum dots embedded in silicon nitride," *Phys. Rev. Lett.* 86(7), 1355-1357 (2001).
- [5]. Mei, J. J., Chen, H., Shen, W. Z. and Dekkers, H. F. W., "Optical properties and local bonding configurations of hydrogenated amorphous silicon nitride thin films," *J. Appl. Phys.* 100(7), 073516 (2006).
- [6]. Negro, L. D., Yi, J. H., Michel, J., Kimerling, L. C., Chang, T. -W. F., Sukhovatkin, V. and Sargent, E. H., "Light emission efficiency and dynamics in silicon-rich silicon nitride films," *Appl. Phys. Lett.* 88(23), 233109

(2006).

- [7]. Sriraman, S., Agarwal, S., Aydil E. S. and Maroudas, D., "Mechanism of hydrogen-induced crystallization of amorphous silicon," *Nature (London)* 418(6893), 62-65 (2002).
- [8]. Chen, H., Shen, W. Z. and Wei W. S., "Structural order effect in visible photoluminescence properties of nanocrystalline Si:H thin films," *Appl. Phys. Lett.* 88(12), 121921 (2006);
- [9]. Chen, X. Y., Shen, W. Z. and He, Y. L., "Enhancement of electron mobility in nanocrystalline silicon/crystalline silicon heterostructures," *J. Appl. Phys.* 97(2), 024305 (2005) ;
- [10]. Pan, W., Lu, J. J., Chen, J. and Shen W. Z., "Resonant tunneling characteristics in crystalline silicon/nanocrystalline silicon heterostructure diodes," *Phys. Rev. B* 74(12), 125308 (2006).
- [11]. Schaller, R. D., Agranovich, V. M. and Klimov, V. I., "High-efficiency carrier multiplication through direct photogeneration of multi-excitons via virtual single-exciton states," *Nature Phys.* 1(3), 189-194 (2005).
- [12]. Beard, M. C., Knutsen, K. P., Yu, P. R., Luther, J. M., Song, Q., Metzger, W. K., Ellingson, R. J. and Nozik, A. J., "Multiple exciton generation in colloidal silicon nanocrystals," *Nano Lett.* 7(8), 2506-2512 (2007).